

Topological Insulator Thin Films Starting from the Amorphous Phase - Bi_2Se_3 as Example

J. Barzola-Quiquia,* T. Lehmann, M. Stiller, D. Spemann, and P. Esquinazi
Institute for Experimental Physics II, University of Leipzig, 04103 Leipzig, Germany

P. Häussler
*Division of Thin Films Physics, Institute of Physics,
 Chemnitz University of Technology, 09107 Chemnitz, Germany*
 (Dated: January 27, 2022)

We present a new method to obtain topological insulator Bi_2Se_3 thin films with a centimeter large lateral length. To produce amorphous Bi_2Se_3 thin films we have used a sequential flash-evaporation method at room temperature. Transmission electron microscopy has been used to verify that the prepared samples are in a pure amorphous state. During annealing the samples transform into the rhombohedral Bi_2Se_3 crystalline structure which was confirmed using X-ray diffraction and Raman spectroscopy. Resistance measurements of the amorphous films show the expected Mott variable range hopping conduction process with a high specific resistance compared to the one obtained in the crystalline phase (metallic behavior). We have measured the magnetoresistance (MR) and the Hall effect (HE) at different temperatures between 2 K and 275 K. At temperatures $T \lesssim 50$ K and fields $B \lesssim 1$ T we observe weak anti-localization in the MR; the Hall measurements confirm the n-type character of the samples. All experimental results of our films are in quantitative agreement with results from samples prepared using more sophisticated methods.

I. INTRODUCTION

Topological insulators (TI) are a new class of materials, which were theoretically predicted to exist in different Bi based materials^{1,2}. Angle-resolved photoemission spectroscopy (ARPES) has been used to verify the topological surface states³⁻⁵ of such materials. TI have, due to strong spin-orbit coupling, an insulating bulk energy gap and generate conducting topologically protected gapless electronic surface states, which are robust against disorder and magnetic impurities⁶.

These new materials have very interesting properties from the basic physics point of view and for future applications, for example the observation of the quantum spin Hall (QSH) effect⁷ or the realization of Majorana fermions for the application in topological quantum computation^{8,9}. The alloy Bi_2Se_3 was proposed² as a three-dimensional (3D) TI, and later it was experimentally confirmed by ARPES¹⁰ that this system possesses a single Dirac fermion at the surface.

Diverse investigations of the transport properties in Bi_2Se_3 were done, e.g. resistance measurements as a function of the temperature verify the metallic surface states¹¹, the Hall effect confirms that Bi_2Se_3 is a n-type carrier and the magnetoresistance shows weak anti-localization (WAL)^{11,12}. The WAL effect is used as evidence that the electrons moving at the surface of the material are time reversal symmetry protected. In a TI the WAL effect is a result of the strong spin-orbit coupling, which, in the presence of defects, puts the backscattering at a minimum when a magnetic field or a magnetic impurity is not present. Under the absence of localization, the surface of a TI remains metallic and is expected to exhibit perfect WAL due to helical surface states^{13,14}. Therefore 2D WAL was used to verify the topological

nature in several cases¹⁵⁻¹⁷, where the temperature dependence of the coherence length l_ϕ is used to prove that the WAL originated from the 2D surface states ($l_\phi \propto T^{0.5}$ for 2D WAL and $l_\phi \propto T^{0.75}$ for 3D WAL)¹⁸.

In the last years tremendous efforts were realized in order to produce this kind of materials as thin films, nanowires, nanocrystals¹⁹ etc., using different techniques such as molecular beam epitaxy (MBE)^{20,21}, metal-organic chemical vapour deposition²² including mechanical exfoliation^{23,24} or chemical vapour transport²⁵. Nevertheless, the preparation of a large area of Bi_2Se_3 films and the possibility to obtain a variety of morphology by the combination with electron beam lithography techniques is still a challenge.

The route of the amorphous-crystalline phase is a powerful method already used to produce high quality thin films of quasicrystalline AlCuFe ²⁶, AlPdMn ²⁷ and AlPdRe ²⁸ samples, whose existence in the phase diagram does not allow variations of more than 2% of the components from the correct concentration. To produce the amorphous films we use a method which allows us to obtain centimeter-large homogeneous samples. The composition of the target material shows a maximum aberration of 1% when compared with the source material. This technique is called the sequential flash-evaporation²⁹ (SFE) and can be easily combined with electron beam lithography to obtain samples in the desired shapes, thickness and can also be used to produce hetero structures, e.g. for the study of proximity effects.

II. EXPERIMENTAL DETAILS

The initial material used for the thin film preparation was commercial Bi_2Se_3 millimetre-large pieces (4–7 mm)

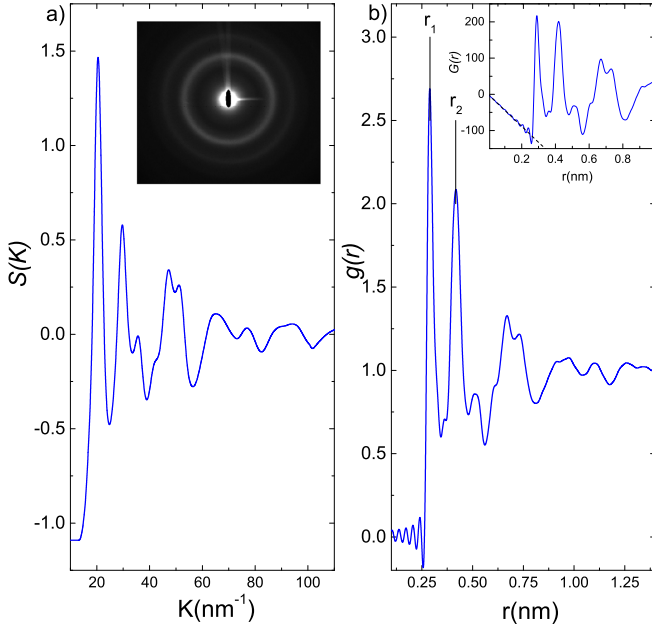


Fig. 1. TEM results, a) structure factor $S(k)$ (the inset shows the TEM picture), b) pair correlation function $g(r)$. The inset shows the reduced atomic distribution function, the linear fit at $r < 0.3$ nm is used to obtain the atomic number density.

from Alfa Aesar with a purity of 99.999%. After milling the pieces to 300–500 μm in diameter, the crushed powder was introduced into the flash evaporation device. The flash evaporation process was done at room temperature under a nominal pressure of $\approx 5 \times 10^{-5}$ mbar. The films for the transport measurements and X-ray analysis were prepared onto Si-substrates ($5 \times 5 \times 0.5$ mm³) coated with an amorphous insulating 150 nm thick Si_3N_4 film.

For transmission electron microscope (TEM) experiments, additional NaCl crystals substrates were placed into the chamber for deposition, which, after dilution in bi-distilled water, left the films floating on the water surface. Thereafter these films were collected onto a commercial TEM Cu-grid. Atomic structure analysis of the initial material and the prepared thin films was measured by means of X-ray diffraction. For TEM measurements we used the transmission electron microscope Philips CM 20 FEG, to obtain the structure factor $S(K)$ and the pair correlation function $g(r)$, we have used a standard method described in³⁰.

The resistance measurements were done using the conventional four point method; in this case the 5×5 mm² size films were structured by scratching using a micro-manipulator. The contacts for low temperature measurements were made out of indium and for the high temperature measurements we used Pd. The ohmic contacts were verified by measuring the I-V curves. First low temperature measurements of the amorphous state were done in a standard commercial closed cycle refrigerator system with a minimal temperature of 25 K. The electrical resistance was measured using a Keithley 6517A electrometer

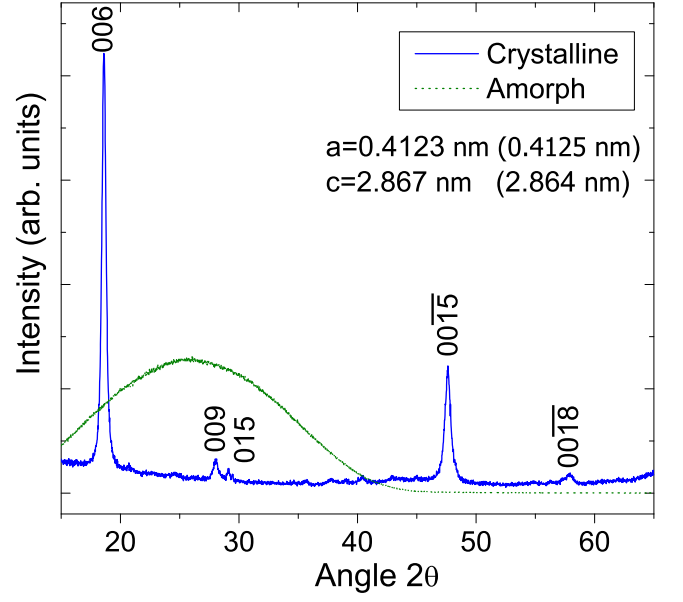


Fig. 2. X-ray diffraction of the crystalline and amorphous thin films. The obtained lattice parameters are in good agreement with the literature values (shown in brackets).

due to the high resistance of the amorphous thin films.

Low-temperature measurements between 2 K and 275 K were realized in a commercial cryostat (Oxford) implemented with a temperature controller (Linear Research LR-700 Bridge) which allows for a temperature stabilization of 5 mK over all temperature range. The cryostat is also equipped with a ± 8 Tesla superconducting magnet, which allows to measure the MR and Hall-effect.

Low-noise resistance measurements have been performed using the AC technique (Linear Research LR-700 Bridge) with ppm resolution. In order to determine the crystallization temperature we used the DC technique (Keithley 2182 with 2001 Nanovoltmeter and Keithley 6221 current source) on the previously structured samples. During the measurements a magnetic field was applied perpendicular to the sample and current, and its value was monitored by a Hall sensor installed close to the sample.

The thickness and stoichiometry of the films were measured with Rutherford backscattering spectroscopy (RBS)³¹ and particle induced x-ray emission (PIXE)³² using a 2.0 MeV proton beam. There is also an increasing interest in the properties of TI materials when magnetic impurities are present. Therefore, the amount of magnetic impurities was quantified using PIXE³² measurements as well. This method provides a high sensitivity, for the samples studied here the typical minimum detection limit is $\approx 2\mu\text{g/g}$. The analysis of the RBS and PIXE spectra was performed using XRUMP³³ GeoPIXE II³⁴. The 2.0 MeV protons used have a penetration depth of $\approx 30\mu\text{m}$ in Bi_2Se_3 and therefore PIXE gives the impurity concentration of all the complete sample if its thickness

is less than this value, as it is in our case.

Raman spectra of the crystalline samples were obtained at room temperature and ambient pressure with a Dilor XY 800 spectrometer at 514.53 nm wavelength (green) and a 2 μm spot diameter. The incident power was varied between 0.5 mW to 3 mW in order to check for possible sample damage or laser induced heating effects. No damage or significant spectral change was observed in this range of incident power.

III. RESULTS AND DISCUSSION

After the SFE preparation process at room temperature, the amorphous samples were obtained. The electron diffraction pattern of the amorphous sample is shown in the inset of Fig. 1. After analysis we obtained the atomic structure factor $S(K)$ and the pair correlation function $g(r)$, both results are plotted in Fig. 1.

The structure results are comparable to known similar amorphous semiconductor systems³⁵, but specially to the structure of the liquid phase of Bi_2Se_3 investigated by Usuki³⁶. Our results show similar features as the liquid phase, e.g. the position of the first and second peak in the $S(K)$ and $g(r)$ are almost at the same values. The first peak at $r_1 \approx 0.29$ nm in $g(r)$ corresponds to the same value in the liquid phase and is close to the corresponding first nearest neighbor distance in the crystalline phase of Bi_2Se_3 ³⁷; the peak $r_2 \approx 4.18$ nm was identified in the liquid phase as consequence of the building of a short-range order related to the crystalline phase³⁶. After integration, the first peak in $g(r)$ allows us to calculate the coordination number $N_c \approx 3.2$. This value is less than that of the liquid state ($N_{c,\text{Liquid}} \approx 4.12$)³⁶ and is due to the amorphous phase, which builds more defined first neighbors in comparison to the liquid phase. From the slope of the reduced atomic distribution $G(r) = 4\pi r n_0 [g(r) - 1]$ at small values of r (dashed line in Fig. 1), we can calculate the atomic number density $n_0 = 35.05 \text{ nm}^{-3}$, which is comparable to the value of the liquid phase when calculated using a simple linear extrapolation of the density of Bi and Se in the liquid state. From the structure results and the high temperature stability of the amorphous phase (discussed later), we can conclude, according to the well established interpretation^{38,39}, that the system is a stabilized electron-phase, which means the formation of a pseudogap at the Fermi energy⁴⁰ is responsible for the high stability. Consequently, the influence on the electronic transport yields a very high resistivity and semiconducting-like behavior as a function of the temperature. After annealing in argon atmosphere to 425 K, the sample transforms into the crystalline phase. In Fig. 2 we present X-ray results of the amorphous and crystallized thin films. In case of the crystalline films we can recognize the peaks corresponding to the rhombohedral $R\bar{3}m$ (D_{3d}^5) structure of the Bi_2Se_3 phase. The calculated lattice parameters are in very good agreement with literature data³⁵ within experimental precision. Using

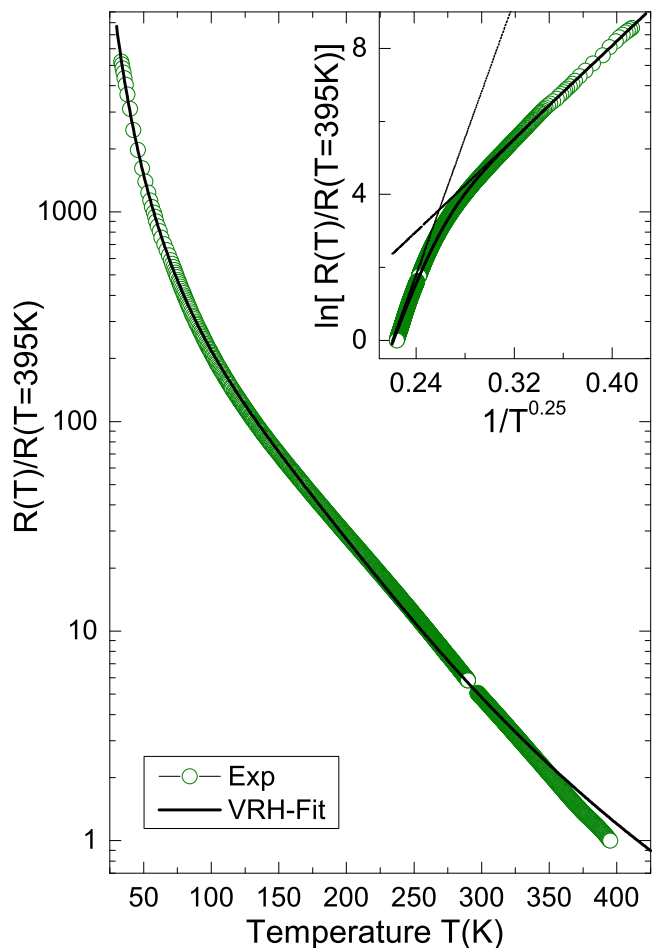


Fig. 3. Resistance vs. temperature of the amorphous sample after preparation at 320 K. The inset shows the fit and the two contributions mentioned in the text.

the Scherrer equation we can determine the crystalline grain size, for that we used the most intense peak and the calculation gives a value of $\approx 19 \pm 2.2$ nm. Taking into account that the unit cell is composed of three layers stacked along the c -axis, each known as quintuple layer (QL), and that a QL has a thickness of ≈ 0.96 nm, our films contain grains which include 20 QLs. That is important because in order to have a Dirac cone it is necessary to have at least 5-6 QL⁴¹. Resistance measurements of the as-prepared amorphous films were also done, the results are shown in Fig. 3. In our device the highest measurable value of the resistance has been reached at 30 K. In the complete temperature range the resistance shows an thermally mechanism, but with two different regimes, which can be seen in two different slopes shown in the inset of Fig. 3. We have found that the temperature dependence of the resistance can be well described by two different variable-range hopping (VHR) conduction processes. The general equation for VRH is given

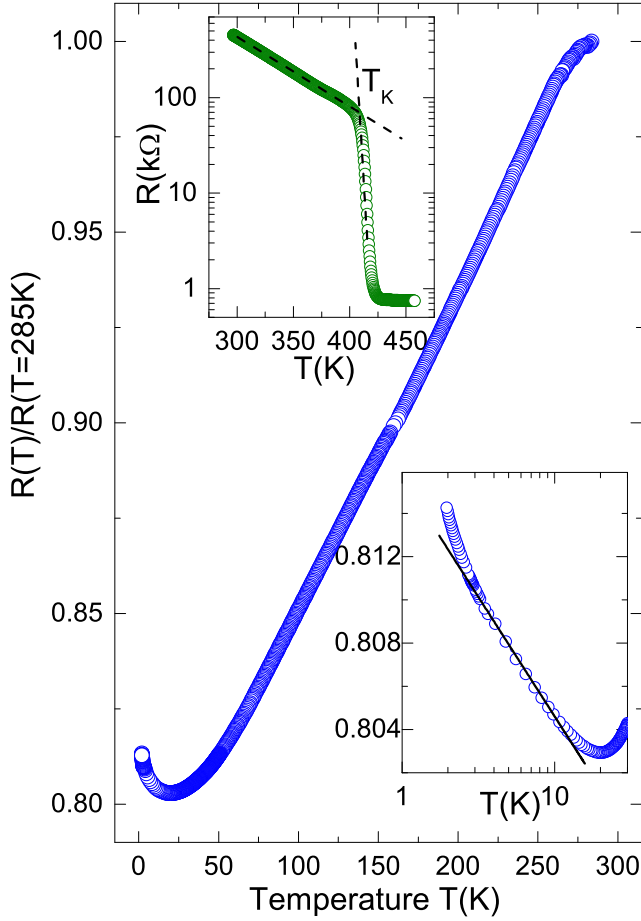


Fig. 4. Resistance vs. temperature from 2 K to 275 K of the crystalline Bi_2Se_3 sample. The upper left inset shows the resistance when the sample transforms from amorphous to crystalline phase, the intersection of the dash lines gives the crystallization temperature T_K . The inset on the r.h.s. shows the resistance of the crystalline sample.

by

$$R(T) = R_0 \cdot \exp \left[\left(\frac{T_0}{T} \right)^p \right], \quad (1)$$

where R_0 is a prefactor and T_0 is a characteristic temperature coefficient. The value of the exponent p depends on the nature of the hopping process. We found that in our amorphous Bi_2Se_3 the value of $p = 0.25$ describes very well the measured transport behavior. This value of p was derived by Mott⁴², and that is in the case of a constant density of states at the Fermi level. According to Mott, T_0 is a coefficient which depends on the density of states $N(E_F)$ at the Fermi level in the form:

$$T_0 = \frac{18}{k_B \xi^3 N(E_F)}, \quad (2)$$

where ξ is the localization length and k_B is the Boltzmann constant. As we mentioned before, it is evident that the resistance in our sample shows two different

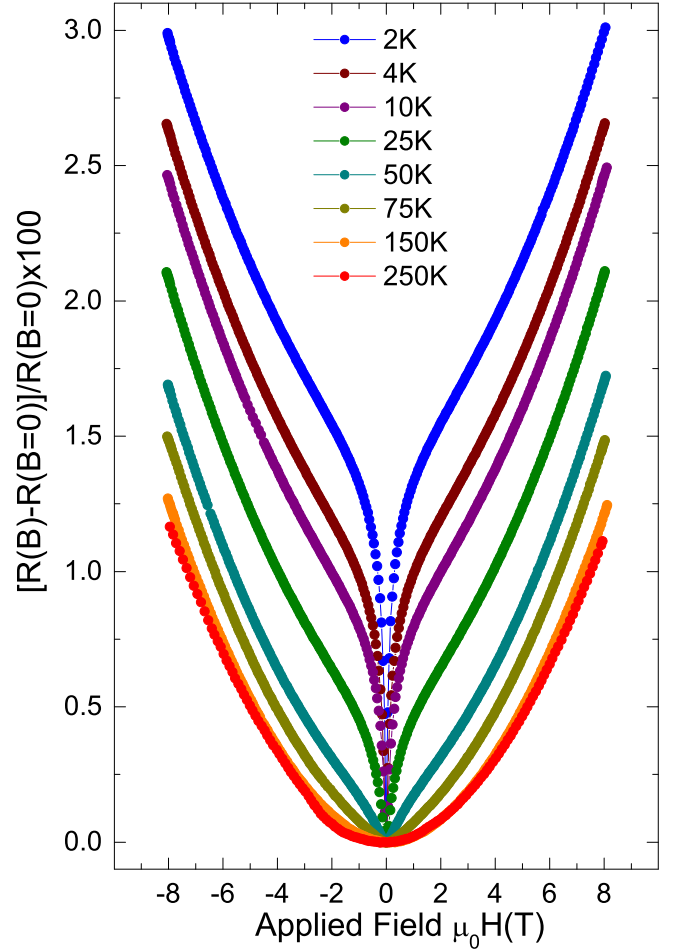


Fig. 5. Magnetoresistance vs. applied magnetic field, measured at different constant temperatures.

temperature regions, in each one the resistance can be described by the Mott-VRH. In order to describe the total temperature dependence we used a simple circuit containing two resistors in parallel which result is shown in Fig. 3 as a line. A deviation of the fit from the experimental data at temperatures $T > 320$ K can be observed because the sample was prepared at ambient temperature and above this value the resistance starts to decrease irreversibly. The contributions of the two resistances are evident in the inset. From the fit we obtain the characteristic temperature T_0 at every region. For the low temperature region $T_{0-LT} = 1.02 \times 10^6$ K and for the high temperature region $T_{0-HT} = 75.87 \times 10^6$ K. Using these values we can estimate the localization length ξ if the value of $N(E_F)$ is known, but this is not yet available in the literature. Assuming a value of the same order for similar amorphous systems, $N(E_F) \approx 10^{20(\pm 1)} \text{eV}^{-1} \text{cm}^{-3}$, we obtain at low temperatures $\xi_{LT} \approx 0.5 \dots 3$ nm and at high temperatures $\xi_{HT} \approx 0.14 \dots 0.6$ nm. These values correspond approximately to the first and second nearest neighbor distances in the pair correlation function obtained from the TEM investigations. By means

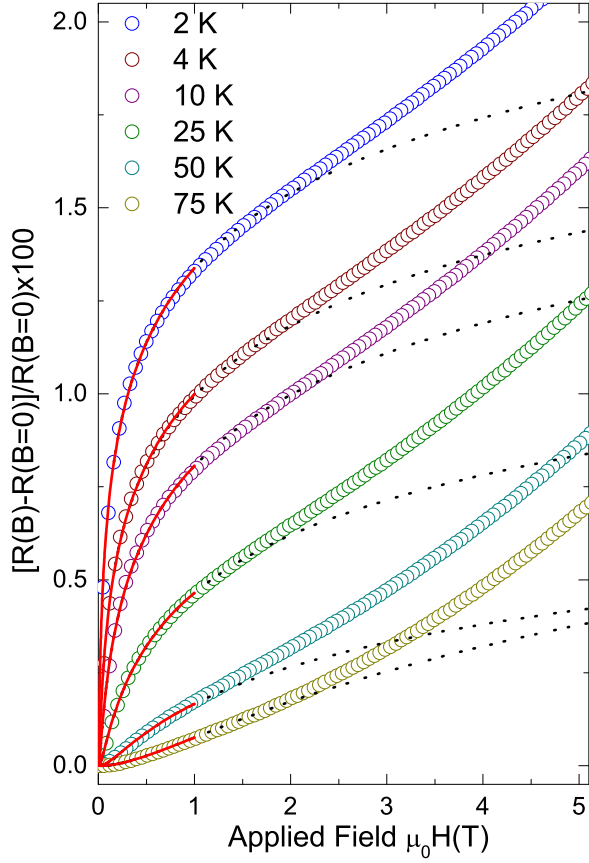


Fig. 6. Low temperature magnetoresistance, the lines show the fits using the WAL theory.

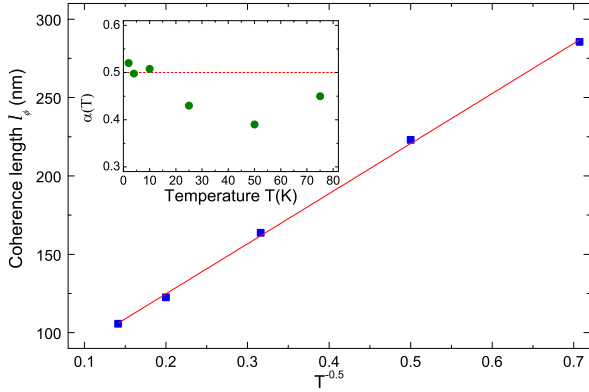


Fig. 7. Coherence length l_ϕ (nm) vs. temperature $T^{-1/2}$ ($K^{-1/2}$) and α (inset) obtained from the fits of the magnetoresistance. The red lines in the figures are the fits and the expected theoretical values of l_ϕ and α respectively.

of the VHR analysis it is difficult to conclude on the reason of the change in the localization length at specific temperature ranges which remains an open question. The transition from amorphous to crystalline phase was monitored by the measurement of the resistance during annealing in a home made device inside an

oven under Ar-flow. The results are shown in the insets of Fig. 4. The crystallization occurs in a nearly step-like process and it is evident that the as-prepared film has a larger resistance in comparison to the crystalline one. The value of the crystallization temperature T_K was determined by intersection of the two lines, one before and another one during the crystallization process. We obtain a T_K of ≈ 410 K, which is relatively high in comparison to amorphous metallic systems^{38,43} but is in the same range of amorphous-like materials such as Al-CuFe^{26,44} and AlPdMn^{45,46}, where a pseudogap at the Fermi energy was observed by means of angular-resolved photoemission studies⁴⁶ and tunneling spectroscopy⁴⁴.

In Fig. 4 we present the results of the temperature dependence of the resistance of our film in the crystalline phase. At temperatures between 15 K and 285 K the sample shows the typical metallic behavior already observed in this system. In the low temperature range $T < 15$ K we observe an increase in the resistance with decreasing T , which nearly follows a logarithmic temperature dependence, as observed in some metals^{47,48} when a small amount of magnetic impurities is present. One possible explanation for this behavior would be an apparent Kondo effect⁴⁹. Note that the resistance increases nearly logarithmic below 12 K. At $T < 3$ K the slope changes which can be a result of the strong influence of the large magnetic impurity content to the spin-orbit interaction characteristic for this system.

As consequence of the resistance behavior at low temperature we did some PIXE measurements. We have analyzed the initial bulk material and the deposited thin film before and after it was transformed from the amorphous phase into the crystalline one. The results of the elements with the highest concentration are summarized in Table I. With the exception of Fe, the concentration of all other magnetic elements was below the detection limit. According to the PIXE results our preparation method has not produced considerable change of the initial stoichiometry. This result confirms the advantages of preparing with the SFE method as before mentioned. According to PIXE, the Fe (Cr) content already present in the initial material has increased more than one order of magnitude after preparation. This contamination can only be due to the milling process before SFE, because the amount in the amorphous and crystalline are quite similar, therefore the contamination in the oven can be ruled out.

In the following we show the results of the transport properties under the application of a magnetic field. In

TABLE I. Results of PIXE measurements.

Sample	Concentration (atom %)	Fe conc. (in ppm)	Cr conc. (in ppm)
Initial mat.	Bi ₄₀ Se ₆₀	34 ± 11	< 29
Amorphous mat.	Bi _{39.4} Se _{60.6}	878 ± 53	319 ± 58
Crystallized mat.	Bi _{40.2} Se _{59.8}	989 ± 48	339 ± 59

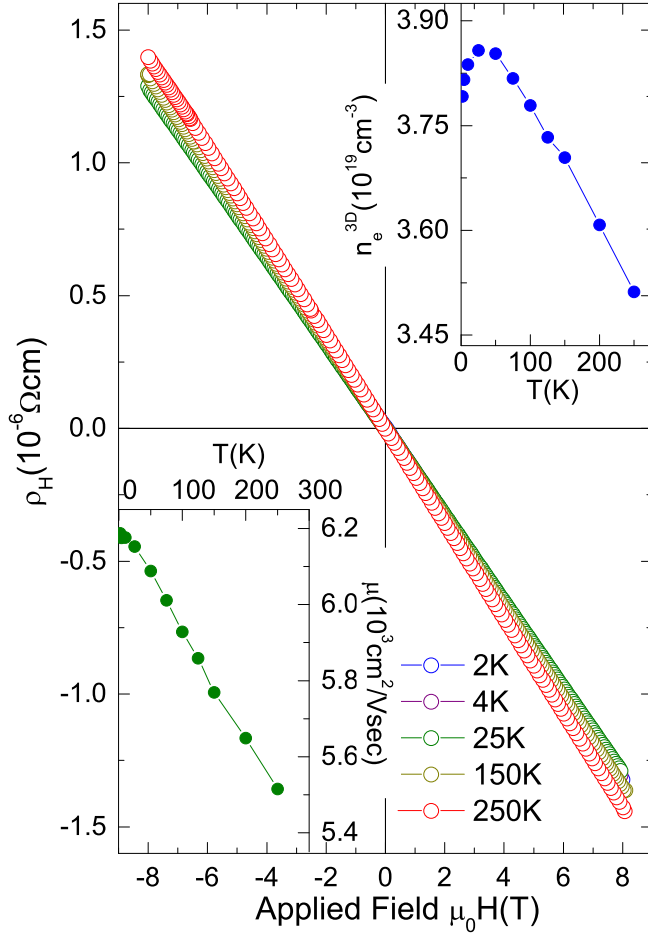


Fig. 8. Hall resistivity vs. applied field at different temperatures. The inset on the l.h.s. shows the calculated mobility, the inset on the r.h.s. the calculated carrier density.

spite of the magnetic impurity content and the large polycrystallinity of the film, the results are quite similar to those reported in the literature for this TI.

The normalized magnetoresistance (MR) is defined as

$$\text{MR} = \frac{R(B) - R(B=0)}{R(B=0)}, \quad (3)$$

and are plotted in Fig. 5. In general the MR is positive for all measured temperatures and at high fields and high temperatures ($B > 1.5$ T, $T > 100$ K) it is dominated by a parabola like dependence, due to the Lorenz force contribution to the carriers scattering under influence of a perpendicular magnetic field⁵⁰. At temperatures $T < 75$ K and in the low-field regime ($B < 1.5$ T) the MR increases sharply as the magnetic field increases, which is the typical behavior of the weak anti-localization (WAL) effect⁵¹. When applying a magnetic field, the time-reversal symmetry breaks down with increasing field strength and the electrons begin to backscatter such that the resistance rises. In order to fit our results with the theory, we define the magnetoconductance (MC) as $\Delta G(B) = G(B) - G(0)$, with $G(0) = 1/R(0)$. The low field part ($B < 1.5$ T) of the MC can be well fitted using

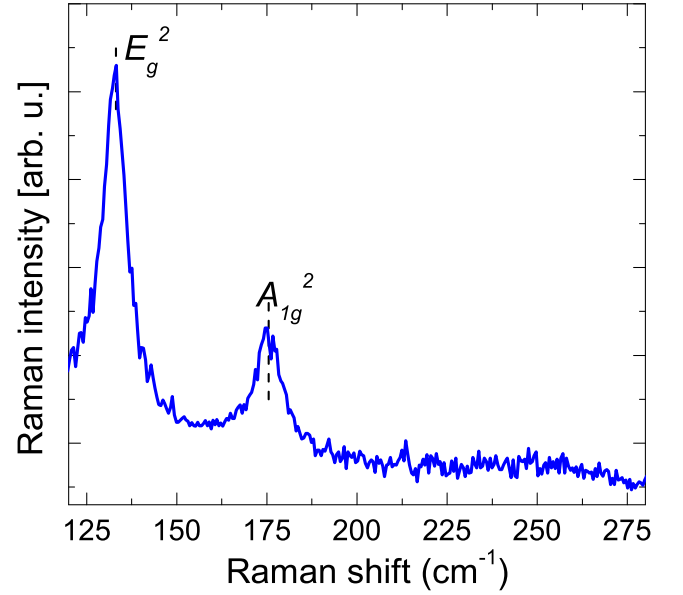


Fig. 9. Raman spectra of the crystalline Bi_2Se_3 sample. The dashed lines indicates the characteristic modes.

the standard WAL theory developed by Hikami-Larkin-Nagaoka, given as:

$$\begin{aligned} \Delta G_{\text{WAL}}(B) &= G(B) - G(0) \\ &= -\alpha \frac{e^2}{\pi^2 \hbar} \left[\psi \left(\frac{1}{2} + \frac{B_\phi}{B} \right) - \ln \left(\frac{B_\phi}{B} \right) \right], \quad (4) \end{aligned}$$

where α is a coefficient whose value was predicted to be $1/2$ in the case of systems with strong spin-orbit interaction, i.e. in the pure WAL regime, ψ is the digamma function, B_ϕ is the dephasing magnetic field related to the phase coherence length l_ϕ according to $B_\phi = \hbar/4el_\phi^2$. Using the Eq. 4, we fit the experimental results, see Fig. 6, and estimate the different parameters at each temperature. The prefactor α and the phase coherence length are shown in Fig. 7. According to our fit results, at the low temperatures ($T < 20$ K), α varies around 0.5 ± 0.2 , which is close to the theoretical expected value. The high temperature values are between 0.38 and 0.45, this can be a consequence of the diminishing of the coherence length with rising temperature. The coherence length varies from 300 nm ($T = 2$ K) to 100 nm ($T = 50$ K), which is in concordance with the value reported for Bi_2Se_3 thin films prepared by molecular beam epitaxy (MBE) with a thickness of 20 QL⁵². According to our results, the temperature dependence of the coherence length is T^b , with $b = 0.51 \pm 0.13$. The exponent gives information about the dimensionality of the system. According to the theory, for a two-dimensional system, $b = 0.5$ and for one dimension, $b = 1/3$. Our result is close to the exponent expected for a two-dimensional system⁵³. For α and the l_ϕ , the observed behavior and values obtained are consistent with that reported for thin films^{52,54,55} and microwires of Bi_2Se_3 ¹².

The Hall measurements were done at the same tem-

peratures as the MR and are presented in Fig. 8. Its sign indicates that the major carriers are electrons, i.e. n-type over the investigated temperature range. From the slope we can calculate the 3D carrier density, the results are plotted in the inset of Fig. 8. The value obtained $n_e^{3D} \approx 3.7 \times 10^{19} \text{cm}^{-3}$ is close to that reported in⁵⁶ where the sample was grown without dopants but also to⁵⁷ where Fe was used as dopant.

According to theoretical predictions, the presence of magnetic impurities in a TI should open a small gap in the surface states due to the breaking of time-reversal symmetry⁵⁸. To verify these predictions experimentally, films containing Fe in unknown concentrations (but with less than 2 % according to the authors^{17,57}) were produced. For all doped samples the results show the typical behavior of the Kondo effect in the temperature dependence of the resistance. The results of the magnetoresistance show the typical WAL behavior and only in samples with a high concentration of Fe, a mix of weak localization (WL) and WAL effects has been seen¹⁷. Anomalous Hall effect was observed in Bi_2Se_3 thin films when doped with Cr, but only when the concentration is $\geq 1.4\%$. Our Hall effect results do not show any sign of an anomalous contribution as a consequence of the Fe and Cr content. Similar results were obtained when Bi_2Se_3 was doped with Fe with a concentration of less than 2 %⁵⁷. We conclude that the amount of Fe and Cr present in our sample apparently does not affect the expected behavior⁵⁸ of the investigated transport properties of the TI.

Finally, in the crystalline state we have done Raman scattering spectroscopy of our films. According to the stoichiometry, the primitive unit cell of Bi_2Se_3 contains five atoms, therefore 15 degrees of freedom are allowed at the center of the Brillouin zone ($q = 0$), from which 3 are acoustic modes and the rest are optical phonons ($2A_{1g}$, $2E_g$, $2A_{1u}$ and $2E_u$). According to previous work³⁷, E_g and A_{1g} modes can be distinguished. In our films we were able to detect the high frequency E_g^2 and A_{1g}^2 modes,

at $\approx 133.14 \text{cm}^{-1}$ and $\approx 175.5 \text{cm}^{-1}$, respectively, see Fig. 9. The measured Raman shift in our samples is in agreement with the results from literature^{37,52}, indicating that our films have similar structural quality as others produced with more sophisticated methods.

IV. CONCLUSION

TI Bi_2Se_3 polycrystalline thin films can be obtained by annealing starting from the amorphous phase. The preparation was done using a simple and inexpensive preparation method, which can also be used to produce similar TI materials, giving the chance to study diverse properties before, during and after the disorder-order transition. The material in the amorphous phase has a high resistivity and behaves like a semiconductor, which transforms in to the metallic crystalline phase at temperatures higher than room temperature. TEM microscopy, X-Ray and RAMAN measurements were used to verify that we have produced the Bi_2Se_3 films in the desired crystalline phase. Using PIXE, a method with high accuracy, we have quantified the presence of magnetic impurities (such as Fe) in the initial material and in the prepared thin films. Nevertheless, despite the films being polycrystalline and that magnetic impurities are present, all measured electronic transport properties characterizing a TI like Bi_2Se_3 were measured and our results are similar to those reported in literature. The fact that our results are quantitatively comparable with data obtained for samples prepared by more sophisticated methods and of apparently much better quality, indicates that: either the surface states are extraordinarily protected and robust against disorder and magnetic impurities, or the results we are comparing are not the ones that one should take as characteristics of a good TI. Future systematic measurements as a function of disorder and magnetic impurities would consequently clarify the amount of disorder and magnetic impurities or both, which causes Bi_2Se_3 to become as a non- TI material.

* j.barzola@physik.uni-leipzig.de

¹ J. Teo, L. Fu, and C. Kane, Phys. Rev. B **78**, 045426 (2008).

² H. Zhang, C. Liu, X. Qi, X. Dai, Z. Fang, and S. Zhang, Nat. Phys **5**, 438 (2009).

³ D. Hsieh and et al., Science **323**, 919 (2009).

⁴ Y. Chen and et al., Science **325**, 178 (2009).

⁵ D. Hsieh and et al., Nature (London) **460**, 1101 (2009).

⁶ M. Liu, J. Zhang, C.-Z. Chang, Z. Zhang, X. Feng, K. Li, K. He, L.-L. Wang, X. Chen, X. Dai, Z. Fang, Q.-K. Xue, X. Ma, and Y. Wang, Phys. Rev. Lett. **108**, 036805 (2012).

⁷ M. König and et al., Science **318**, 766 (2007).

⁸ M. Hasan and C. Kane, Rev. Mod. Phys. **82**, 3045 (2010).

⁹ X.-L. Qi and S.-C. Zhang, Rev. Mod. Phys. **83**, 1057 (2011).

¹⁰ Y. Xia, D. Qian, D. Hsieh, L. Wray, A. Pal, H. Lin, A. Bansil, D. Grauer, Y. Hor, R. Cava, and M. Hasan, Nat. Phys. **5**, 398 (2009).

¹¹ Y. Kim, M. Brahlek, N. Bansal, E. Edrey, G. Kapilevich, K. Iida, M. Tanimura, Y. Horibe, S.-W. Cheong, and S. Oh, Phys. Rev. B **84**, 073109 (2011).

¹² S. Matsuo, T. Koyama, K. Shimamura, T. Arakawa, Y. Nishihara, D. Chiba, K. Kobayashi, and T. Ono, Phys. Rev. B **85**, 075440 (2012).

¹³ S. Hikami, A. Larkin, and Y. Nagaoka, Prog. Theor. Phys. **63**, 707 (1980).

¹⁴ K. Nomura, M. Koshino, and S. Ryu, Phys. Rev. Lett. **99**, 146806 (2007).

¹⁵ L. Bao and et al, Sci. Rep. **2**, 1212 (2012).

- ¹⁶ W. Ning, H. Du, F. Kong, J. Yang, Y. Han, M. Tian, and Y. Zhang, *Sci. Rep* **3**, 1564 (2013).
- ¹⁷ J. Cha, M. Claassen, D. Kong, S. Hong, K. Koski, X.-L. Qi, and Y. Cui, *Nano Letters* **12**, 4355 (2012).
- ¹⁸ B. Altshuler, A. Aronov, and D. Khmelnitsky, *J. Phys. C* **15(36)**, 7367 (1982).
- ¹⁹ S. Zhao, C. Beekman, L. Sandilands, J. Bashucky, D. Kwok, N. Lee, A. D. LaForge, S. W. Cheong, and K. S. Burch, *Appl. Phys. Lett.* **98**, 141911 (2011).
- ²⁰ G. Zhang and et al., *Adv. Funct. Mater.* **21**, 2351 (2011).
- ²¹ M.-X. Wang and et al., *Science* **336**, 52 (2012).
- ²² Y.-F. Lin and et al., *J. Phys. Chem. C* **111**, 18538 (2007).
- ²³ J. Checkelsky and et al., *Phys. Rev. Lett.* **103**, 246601 (2009).
- ²⁴ D. Hsieh and et al., *Nature* **460**, 1101 (2009).
- ²⁵ W. Jiao, S. Jiang, C. Feng, Z. Xu, G. Cao, M. Xu, D. Feng, A. Yamada, K. Matsubayashi, and Y. Uwatoko, *AIP Advances* **2**, 022148 (2012).
- ²⁶ C. Roth, G. Schwalbe, R. Knöfler, F. Zavaliche, O. Madel, R. Haberkern, and P. Häussler, *Journal of Non-Crystalline Solids* **252**, 869 (1999).
- ²⁷ R. Haberkern, J. Barzola-Quiquia, C. Madel, and P. Häussler, *MRS Proceedings* **K8.3**, 643 (2000).
- ²⁸ R. H. and K. Khedri, C. Madel, and P. Häussler, *Materials Science and Engineering*, 294 (2000).
- ²⁹ P. Häussler, *Topics Appl. Phys.* **72**, 163 (1994).
- ³⁰ H. Leitz, *Z. Phys. B* **40**, 65 (1980).
- ³¹ W. Chu, J. Mayer, and M. Nicolet, *Backscattering Spectrometry* (Academic Press, New York, 1978).
- ³² S. Johansson, J. Campbell, and K. Malmqvist, *Particle-Induced X-Ray Emission Spectrometry* (John Wiley & Sons, Inc., New York, 1995).
- ³³ L. Doolittle, *Nucl. Instr. Meth. B* **9**, 344 (1985).
- ³⁴ C. Ryan, *Nucl. Instr. Meth. B* **181**, 170 (2001).
- ³⁵ J. Barzola-Quiquia and P. Häussler, *Journal of Non-Crystalline Solids*, 299 (2002).
- ³⁶ T. Usuki, Y. Shirakawa, K. Maruyama, and S. Tamaki, *Journal of Non-Crystalline Solids* **716**, 156 (1993).
- ³⁷ W. Richter, H. Köhler, and C. Becker, *Phys. Stat. Sol. B* **84**, 619 (1997).
- ³⁸ P. Häussler, *Phys. Rep.* **222**, 65 (1992).
- ³⁹ J.B.-Quiquia and P. Häussler, *Journal of Non-Crystalline Solids* **299–302**, 269 (2002).
- ⁴⁰ P. Häussler, *Topics in Appl. Phys.* **72**, 163 (1994).
- ⁴¹ Y. Zhang, K. He, C.-Z. Chang, C.-L. Song, L.-L. Wang, X. Chen, J.-F. Jia, Z. Fang, X. Dai, W.-Y. Shan, S.-Q. Shen, Q. Niu, X.-L. Qi, S.-C. Zhang, X.-C. Ma, and Q.-K. Xue, *Nature Physics* **6**, 584 (2010).
- ⁴² N. F. Mott, *J. Non-Cryst. Solids* **1**, 1 (1968).
- ⁴³ J.B.-Quiquia, M. Lang, D. Decker, and P. Häussler, *J. Non-Cryst. Sol.* **334–335**, 352 (2004).
- ⁴⁴ T. Schaub, J. Delahaye, C. Gignoux, C. Berger, G. Fourcaudot, F. Giroud, T. Grenet, and A. Jansen, *Jour. of Non-Cryst. Sol.* **250–252**, 874 (1999).
- ⁴⁵ R. Haberkern, J.B.-Quiquia, C. Madel, and P. Häussler, *Mater. Res. Soc. Symp.* **643**, K8.31 (2001).
- ⁴⁶ X. Wu, S. Kycia, C. Olson, P. Benning, A. Goldman, and D. Lynch, *Phys. Rev. Lett.* **75**, 4540 (1995).
- ⁴⁷ K. Fischer, *Z. Phys. B-Cond. Matter* **42**, 27 (1981).
- ⁴⁸ H.-T. He, G. Wang, T. Zhang, I.-K. Sou, G. Wong, and J.-N. Wang, *Phys. Rev. Lett.* **106**, 166805 (2011).
- ⁴⁹ J. Kondo, *Prog. Theor. Phys.* **32**, 37 (1964).
- ⁵⁰ C. Hurd, *The Hall effect in Metals and Alloys* (Plenum New York, 1972).
- ⁵¹ S. Hikami, A. Larkin, and Y. Nagaoka, *Prog. Theor. Phys.* **63**, 707 (1980).
- ⁵² Y. Kim, X. Chen, Z. Wang, J. Shi, I. Miotkowski, Y. Chen, P. Sharma, A. L. Sharma, M. Hekmaty, Z. Jiang, and D. Smirnov, *App. Phys. Lett.* **100**, 071907 (2012).
- ⁵³ J. Chen, H. Qin, F. Yang, J. Liu, T. Guan, F. Qu, G. Zhang, J. Shi, X. Xie, C. Yang, K. Wu, Y. Li, and L. Lu, *Phy. Rev. Lett.* **105**, 176602 (2010).
- ⁵⁴ J. Wang, A. DaSilva, C.-Z. Chang, K. He, J. Jain, N. Samarth, X.-C. Ma, Q.-K. Xue, and M. Chan, *Phys. Rev. B* **83**, 245438 (2011).
- ⁵⁵ Y. Onose, R. Y. A. Tsukazaki, H. Yuan, T. Hidaka, Y. Iwasa, M. Kawasaki, and Y. Tokura, *Appl. Phys. Express* **4**, 083001 (2011).
- ⁵⁶ J. Analytis, J.-H. Chu, Y. Chen, F. Corredor, R. McDonald, Z. Shen, and I. Fisher, *Phys. Rev. B* **81**, 205407 (2010).
- ⁵⁷ J. Cha, J. Williams, D. Kong, S. Meister, H. Peng, A. Bestwick, P. Gallagher, D. Goldhaber-Gordon, and Y. Cui, *Nano Letters* **10**, 1076 (2010).
- ⁵⁸ Q. Liu, C.-X. Liu, C. Xu, X.-L. Qi, and S.-C. Zhang, *Phys. Rev. Lett.* **102**, 156603 (2009).